RESEARCH ARTICLE

NANO · MICRO small
www.small-journal.com

Long-Term Selective Photoelectrochemical Glycerol Oxidation via Oxygen Vacancy Modulated Tungsten Oxide with Self-Healing

*Yoonsung Jung, Seunghwan Kim, Seungkyu Kim, Yejoon Kim, Jun Beom Hwang, Dong-Yu Kim, and Sanghan Lee**

The photoelectrochemical selective oxidation of biowaste glycerol into the high value-added material, along with hydrogen production, holds significant promise for advancing renewable and sustainable energy technologies. Here, the surface oxygen state of tungsten oxide is modified to selectively oxidize glycerol into glyceraldehyde, a high-value-added material, and the selectivity is maintained over a prolonged period using the photo-stimulated self-recovery capability. The surface-coordinated photoelectrode exhibits high charge transfer efficiency to glycerol and favorable glycerol adsorption capacity, enabling the selective conversion of glycerol. At 1.2 V_{RHE} in a 2 M glycerol electrolyte adjusted to pH 2, the tungsten oxide photoelectrode achieves a photocurrent density of 2.58 mA cm^{-2} and a production rate of 378.8 mmol m^{-2} h^{-1} with selectivity of 86.1%. The high selectivity is preserved for 18 h by utilizing the self-healing capability of tungsten oxide to restore initial states modified by photoelectrochemical oxidation. This work sheds light on the design of highly efficient metal oxide photoelectrodes for selective biomass oxidation over extended periods.

1. Introduction

In an electrochemical hydrogen production system, oxidizing excess biomass into high-value-added products instead of splitting water and producing oxygen provides environmental and economic benefits.[1] Glycerol, a low-value biomass byproduct of biodiesel, has the potential to be converted into high-value-added products due to its highly functionalized molecular structure. Efficient and selective conversion of glycerol is critical to improving the economic and environmental benefits of biodiesel, which is increasingly used as a renewable energy source to mitigate fuel depletion and environmental pollution.[2] Photoelectrochemical oxidation is an environmentally friendly and sustainable energy conversion system that can produce value-added products from glycerol. Among several glycerol conversion methods, it shows the most promise due to its ability to produce versatile oxygenated compounds, facilitate efficient anodic oxidation of organic compounds via direct electron transfer, and simultaneously enable the formation of cathodic hydrogen.[3] Furthermore, photoelectrochemical oxidation systems obviate the necessity for severe conditions such as high temperatures, high pressures, or exogenous oxidants, as well as the complicated separation and disposal procedures required by thermocatalytic or enzyme-catalyzed systems.[4]

Glycerol can be converted by partial oxidation to products such as glyceraldehyde (GAD), dihydroxyacetone (DHA), glycolic acid, glyceric acid, oxalic acid, and formic acid. Among these products, GAD and DHA have the highest value.[5] Specifically, GAD is used as a skincare ingredient in the cosmetics industry and serves as an antibiotic or anticancer agent in pharmaceutical products.[6] Moreover, glycerol is readily oxidized to GAD compared to water, making it a favorable candidate for photoelectrochemical oxidation reactions. This preference stems from the thermodynamic driving force of the conversion of glycerol to GAD, with an E_{eq} = 0.206 V_{SHE}, which is lower than the E_{eq} = 1.23 V_{SHE} required for the conversion of water to oxygen.[7] However, the selective conversion of glycerol to GAD is challenging because GAD is produced during the initial stages of the glycerol reaction pathway. In contrast, C3 products like glyceric acid, C2 products such as glycolic acid and oxalic acid, and C1 products including acetic acid, formic acid, and CO_2 are produced in the later stages. Moreover, the thermodynamic driving favors the formation of more stable peroxidation products, such as carbon dioxide, with an E_{eq} = 0.003 V_{SHE}.[1] Additionally, the reactivity of hydroxyl groups

Y. Jung, S. Kim, S. Kim, Y. Kim, J. B. Hwang, D.-Y. Kim, S. Lee
School of Materials Science and Engineering
Gwangju Institute of Science and Technology (GIST)
123 Cheomdan-gwagiro, Buk-gu, Gwangju 61005, Republic of Korea
E-mail: sanghan@gist.ac.kr

S. Lee
Research Center for Innovative Energy and Carbon Optimized Synthesis for Chemicals (Inn-ECOSysChem)
Gwangju Institute of Science and Technology (GIST)
123 Cheomdan-gwagiro, Buk-gu, Gwangju 61005, Republic of Korea

The ORCID identification number(s) for the author(s) of this article can be found under https://doi.org/10.1002/smll.202409082

DOI: 10.1002/smll.202409082

in glycerol complicates the determination of the reaction pathway, further hindering the achievement of selective conversion.[8] During long-term reactions, these interferences amplify the difficulty of regulating glycerol's reactivity.

Recently, surface modifications, such as adjusting the electronic structure to regulate the behavior of photogenerated charge carriers or adjusting the configuration of surface atoms to regulate the adsorption and desorption of substrates have attracted attention to control glycerol conversion.[8–9] Modulation of the electrode surface can be accomplished by the introduction of defect control,[10] dictated by crystal facets,[11] the incorporation of noble metals,[12] coordination of co-catalysts,[13] surface doping,[14] etc. Oxygen vacancy management is an effective defect control strategy to improve the photoelectrochemical performance of metal oxide semiconductors by modifying light absorption, charge separation, charge transport, electrical conductivity, and surface adsorption.[15] Furthermore, the structural arrangement of the oxygen atoms on the metal oxide surface influences the composition of Lewis and Brønsted acid sites, which are important for selectively reacting organic reactants such as glycerol.[16] Therefore, promoting glycerol oxidation and selective partial oxidation in metal oxide-based semiconductors hinges on the adjustment of the optimal oxygen vacancy concentration.

In this study, tungsten oxide nanostructures synthesized via hydrothermal methods underwent heat treatment and surface reactions to achieve an optimal oxygen vacancy concentration, enabling the selective conversion of glycerol to GAD. The surface oxygen vacancy-modulated tungsten oxide improved charge transfer efficiency without the charge trapping effect of oxygen vacancies, increasing the photocurrent density of 1.70 mA cm^{-2} at 1.2 V_{RHE} with 94.5% selectivity, and enhancing production rate to 315.1 mmol m^{-2} h^{-1}. This highlights that the arrangement of oxygen vacancies on the surface is crucial for glycerol selectivity. Furthermore, to sustain selective reactions over long-term durations, the surface alterations of the photoelectrode were analyzed. By leveraging the photo-stimulated self-healing capability of the photoelectrode to restore its surface state to pre-reaction, the selectivity retention threshold at 1.2 V_{RHE} was extended from 3 to 18 h, achieving an average selectivity of 86.1% with a photocurrent density of 2.58 mA cm^{-2} and a production rate of 378.8 mmol m^{-2} h^{-1}.

2. Results and Discussion

2.1. Preparation and Structural Characterization of Tungsten Oxides

The nanostructured tungsten oxide served as the photoelectrode for the oxidation of glycerol (**Figure 1a**). To achieve efficient conversion from glycerol to GAD, oxygen vacancies were controlled through heat treatment and $NaBH_4$ treatment. The hydrothermally synthesized orthorhombic phase of $WO_3 \bullet H_2O$ on the fluorine-doped tin oxide (FTO) substrate was subjected to a heat treatment process to transform it into a monoclinic phase of WO_{3-x} phase while modulating the oxygen vacancy in the bulk by controlling the ratio of oxygen (O_2) and argon (Ar) gas in the heat treatment environment (Figure S1, Supporting Information).[17] The tungsten oxide subjected to annealing exclusively in an oxygen environment is designated as WO_3. Among the tungsten, oxides annealed in an environment of O_2 and Ar gas mixture to create vacancies, the tungsten oxide that demonstrated the most favorable glycerol conversion under the atmosphere of 1 vol% O_2 and 4 vol% Ar was designated as WO_3(A). For the exclusive formation of oxygen vacancies solely on the surface of WO_3, the WO_3 treated with 15 mM $NaBH_4$, which demonstrated the most optimal surface vacancy formation among various $NaBH_4$ concentrations, was designated as WO_3(S).

The scanning electron microscopy (SEM) analysis was conducted to confirm the absence of morphological changes during the vacancy adjustment. The SEM topography displayed in Figure S2 (Supporting Information) reveals that the tungsten oxide morphology remains unaffected by the heat treatment environment, with no discernible morphological differences between WO_3 annealed in an oxygen environment and WO_3(A) with optimal oxygen vacancy. Similarly, the structure of WO_3(S) with the optimal oxygen vacancy formed by the surface reaction shows no discernible differences (Figure 1b). Consequently, all tungsten oxides synthesized through hydrothermal methods exhibit 1 µm-sized structures oriented perpendicular to the FTO substrate (Figure 1c). These configurations, distinguished by a larger surface area compared to the flat structure, significantly contribute to the improved efficiency of glycerol oxidation. In Figure 1d, the results of the structural analysis of tungsten oxide using transmission electron microscopy (TEM) are presented, providing valuable insights into its nanostructures. The TEM images of WO_3(S) nanostructures reveal distinct lattice fringes, indicating their high crystallinity. For a more detailed analysis of the surface structure, Figure 1e,f presents the zoomed-in image and the resulting fast Fourier transform (FFT). The predominant portion of WO_3 demonstrates high crystallinity, with d-spacings of 0.38 and 0.36 nm, corresponding to the (002) and (200) crystal orientations, respectively.[17a] The same crystal orientation is also observed in WO_3 and WO_3(A) (Figure S3, Supporting Information). On the other hand, the amorphous layer on the surface of WO_3 is 0.6 nm, while WO_3(A) and WO_3(S) exhibit a thicker 1.0 nm amorphous layer which could facilitate optimal vacancy formation. Correspondingly, the FFT image reveals clearer periodic reflection points in WO_3 compared to WO_3(A) and WO_3(S), where they appear more indistinct due to a wider amorphous section. To further verify that the surface layer is amorphous, FFT images were analyzed from 1 nm-sized regions within both the amorphous and crystalline layers in the enlarged image (Figure S4, Supporting Information). The FFT of the tungsten oxide interior exhibited distinct periodic reflection points, confirming the crystalline of the region, whereas no such points were observed in the FFT of the surface, confirming its amorphous structure. The increase in surface oxygen vacancy led to the collapse of the lattice structure, transforming the surface section into an amorphous layer.

X-ray diffraction (XRD) was performed to investigate the structural changes of tungsten oxide during vacancy formation. As shown in **Figure 2a**, all diffraction peaks correspond to monoclinic tungsten oxide phases, except for the FTO peak marked with an asterisk, and no other multiphase structure was detected. It is a polycrystalline phase composed of various crystal planes. The primary crystal planes, (002), (020), and (200), are located at 23.1, 23.6, and 24.4°, respectively, displaying strong

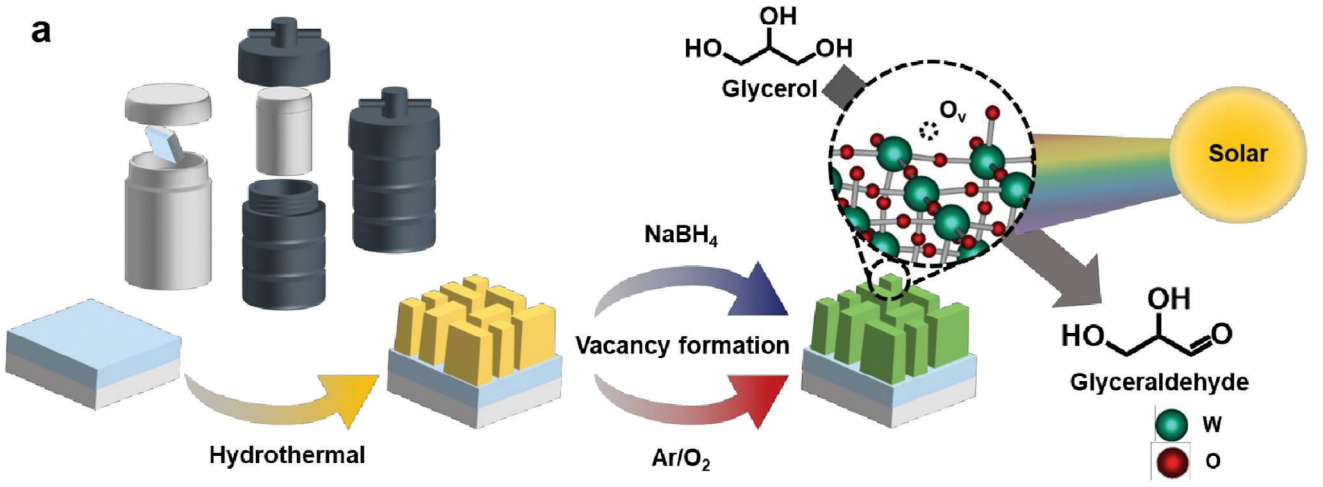

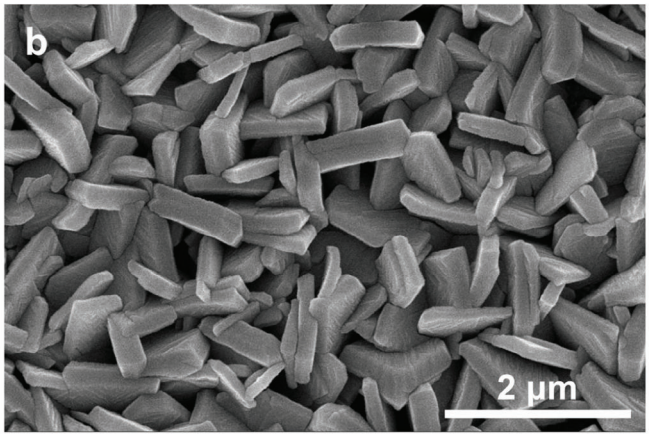

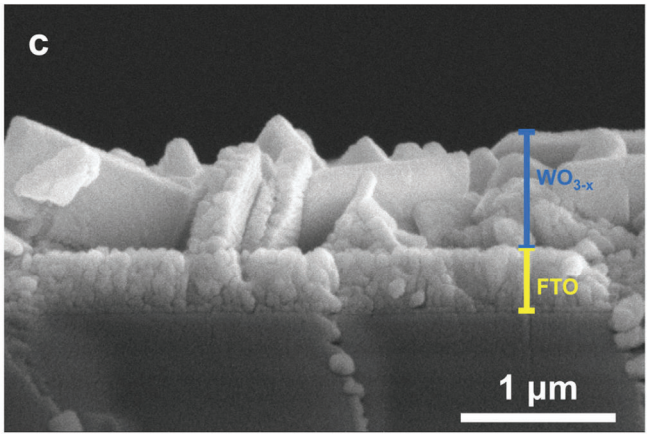

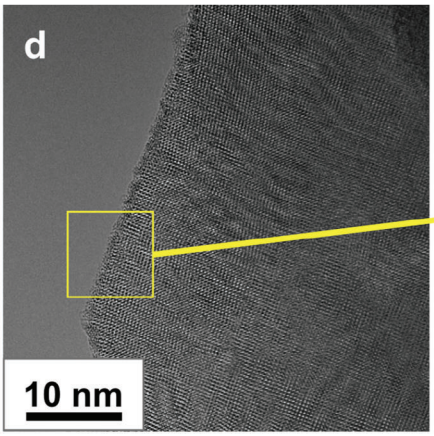

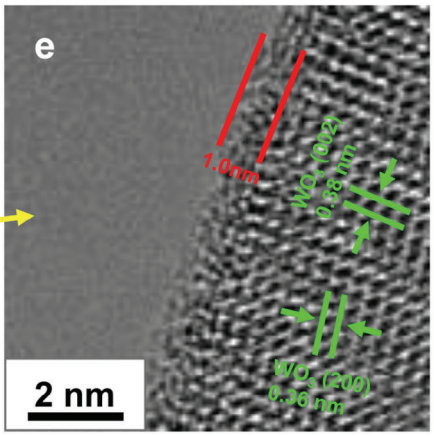

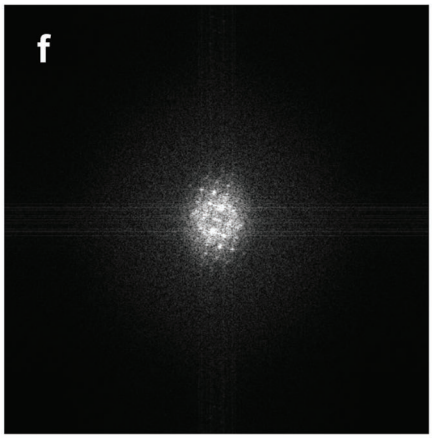

Figure 1. a) Schematic illustration for preparation of surface oxygen vacancy modulated tungsten oxide electrodes. b,c) SEM images of the WO_3(S) nanostructure. d,e) High-resolution TEM image of an individual WO_3(S) nanosheet showing lattice fringes of WO_3(S). f) Corresponding FFT of the yellow-colored region.

intensities. These observations confirm that tungsten oxide is a highly crystalline phase. After heat treatment, WO_3(A) maintains the same crystal phase as WO_3. However, in the WO_3(S), the representative crystal orientation shifted to (001) as the (100) crystal orientation was diminished due to surface layer amorphization. This shift in the representative crystalline orientation, induced by amorphization, is evident in Figure S1 (Supporting Information). When heat treatment was conducted using only Ar gas to form a maximum oxygen vacancy concentration rather than the optimal oxygen vacancy concentration, the $WO_3 \cdot H_2O$ phase disappeared from the XRD pattern, and the crystallinity decreased, accompanied by changes in the representative crystalline signal.

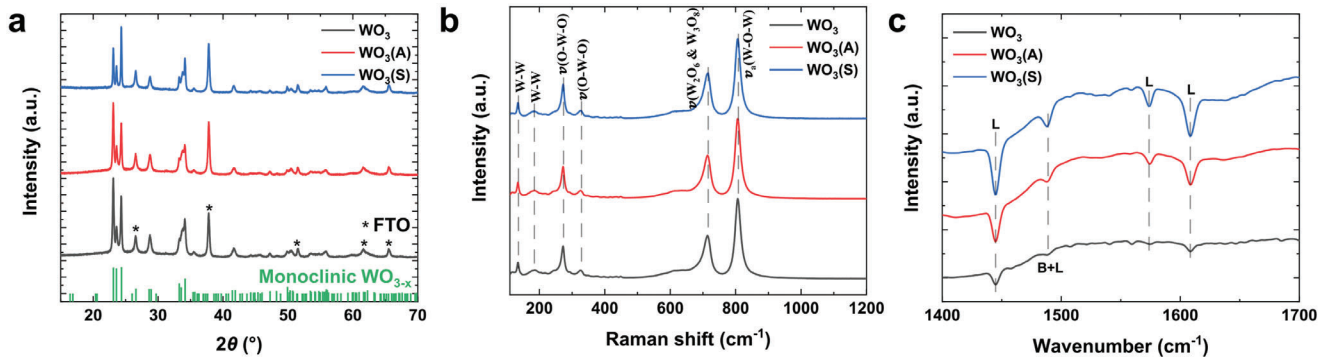

Figure 2. a) XRD patterns of WO_3, WO_3 (A), and WO_3 (S). b) Raman scattering spectra of WO_3, WO_3 (A), and WO_3 (S). c) FTIR spectra of WO_3, WO_3 (A), and WO_3 (S).

This suggests that the high oxygen vacancy concentration hinders crystallization and potentially influences the representative crystalline structure.

Figure 2b presents the Raman scattering spectra, with all bands corresponding to tungsten oxide. The signal at 134 cm^{-1} corresponds to deformation modes, while the signal at 184 cm^{-1} corresponds to stretching modes.[18] Signals below 200 cm^{-1} are attributed to lattice modes. The stretching vibrations of bridging oxygen correspond to the antisymmetric stretch of W—O—W bonds, attributed to the peaks at 714 and 806 cm^{-1} with a shoulder peak at 610 cm^{-1}. The sharp and intense peaks in the stretching vibrations are characteristic of the monoclinic crystalline phase of tungsten oxide. The bending vibration of bridging oxygen corresponds to the symmetric stretch of O—W—O bonds, attributed to the peaks at 272 and 326 cm^{-1}. The intense and sharp peak at 272 cm^{-1}, similar to the XRD results, indicates that the tungsten oxides exhibit a well-defined crystalline phase.[18a]

Fourier-transform infrared (FTIR) analysis was conducted to quantify the concentration of surface acid sites on the tungsten oxide. The type and quantity of acid sites were determined by examining the signal of pyridine adsorbed on the surface of tungsten oxide (Figure 2c). The signals at 1444, 1488, 1574, and 1610 cm^{-1} are attributed to the chemisorption of pyridine on surface Lewis acid sites.[16,19] WO_3(S) exhibited the highest peak intensity for Lewis acid sites, indicating the greatest number of unsaturated tungsten atoms on its surface, followed by WO_3(A) and WO_3, with vacancy formation occurring through a surface reaction. On the other hand, Brønsted acid sites can develop on the surface of tungsten oxide in acidic environments where hydrogen protons are abundant.[20] The FTIR spectra of tungsten oxide immersed for 30 min in an electrolyte used in photoelectrochemical reactions containing sulfuric acid revealed new signals at 1540 and 1636 cm^{-1}, attributed to Brønsted acid sites (Figure S5, Supporting Information).[19] Moreover, the peak at 1574 cm^{-1}, where the two acid sites overlap, exhibited a stronger signal intensity. Therefore, the ratio of acid sites was fine-tuned by controlling the concentration of Lewis acid sites through the regulation of surface vacancy concentration and the formation of Brønsted acid sites in the acidic electrolyte. This precise control allows for the optimization of tungsten oxide's surface properties for specific catalytic and photoelectrochemical applications.

2.2. Surface Characterization of Tungsten Oxides

Figure 3 and Table S1 (Supporting Information) present the concentration of oxygen vacancies and the chemical state on the surface of tungsten oxide using X-ray photoelectron spectroscopy (XPS) analysis. The high-resolution XPS spectra of O1s reveal a lattice oxygen (O_L) peak at ≈530 eV, a peak at ≈531 eV attributed to oxygen vacancies (O_V), and a peak at ≈532.5 eV, attributed to chemisorbed oxygen (O_C), such as water.[15a,21] For WO_3 and WO_3(A), the O_C signal is weak due to the removal of chemisorbed oxygen after heat treatment. However, in the case of WO_3(S), exposure to a water environment during sodium borohydride treatment leads to an intensified chemisorbed oxygen signal. An expansion in the O_V area indicates an increase in the concentration of oxygen vacancies resulting from surface modulation. The concentration of oxygen vacancies is highest in WO_3(S) (21.4%), followed by WO_3(A) (17.2%) and WO_3 (12.4%). This apparent oxygen vacancy concentration ratio becomes even more pronounced when chemisorbed oxygen is excluded. (Table S1, Supporting Information) This variation in vacancy concentration results in distinct ratios of W^{6+}, associated with lattice oxygen, and W^{5+}, associated with oxygen vacancy defects, in the high-resolution XPS spectra of the W4f orbital. The peaks at 35.7 and 37.8 eV correspond to the $4f_{7/2}$ and $4f_{5/2}$ orbitals of W^{6+}, while the peaks at 34.5 and 36.7 eV correspond to the $4f_{7/2}$ and $4f_{5/2}$ orbitals of W^{5+}.[15b,21] The W 5p orbital appears at 41.6 eV. With changes in oxygen vacancies, the concentration ratios of W^{5+} to W^{6+} in the W4f orbitals are 6.0% to 94.0% for WO_3, 7.4% to 92.6% for WO_3(A), and 8.1% to 91.9% for WO_3(S). This indicates that the area of W^{5+} expands compared to W^{6+} due to the increase in oxygen vacancy concentration. Therefore, the increase in the percentage of orbitals related to oxygen vacancies in the O1s and W4f orbitals indicates the successful formation of oxygen vacancies on the surface.

Additionally, the survey XPS spectra presented in Figure S6 (Supporting Information) demonstrate the absence of bands associated with boron, indicating that the surface reaction process employed to produce WO_3(S) did not involve boron doping but solely led to vacancy formation.[22] Electron spin resonance (ESR) spectroscopy was conducted to confirm the presence and concentration of oxygen vacancies (Figure 3g). The excess electrons in the metal oxide are primarily localized at the oxygen vacancy sites, leading to signals at a g factor of 2.00.[23] The signal

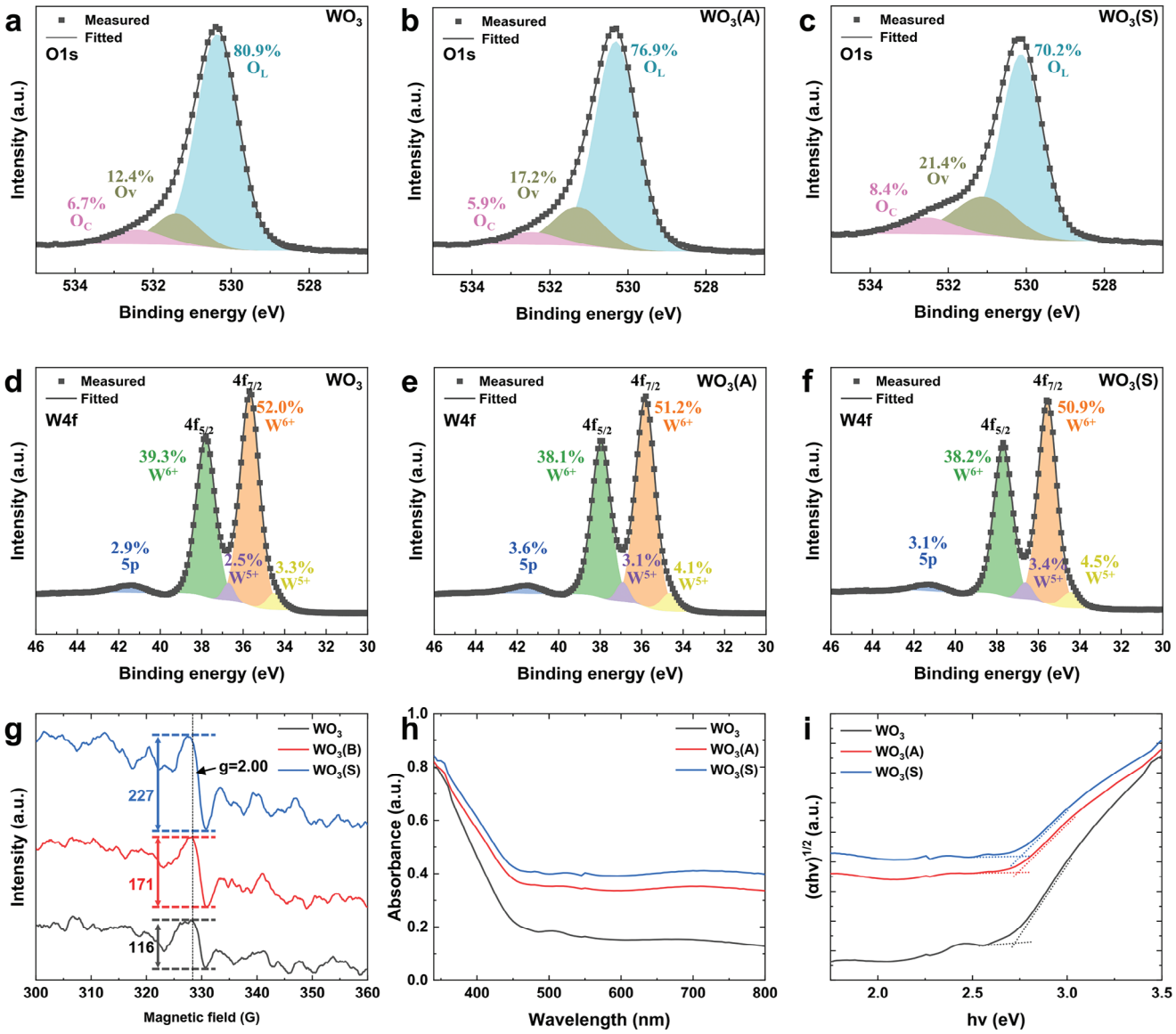

Figure 3. a) High-resolution O1s XPS spectra of WO_3. b) High resolution O1s XPS spectra of WO_3(A). c) High resolution O1s XPS spectra of WO_3(S). d) High resolution W4f XPS spectra of WO_3. e) High resolution W4f XPS spectra of WO_3(A). f) High resolution W4f XPS spectra of WO_3(S). g) ESR spectra of WO_3, WO_3(A), and WO_3(S). h) UV–vis–NIR spectra of WO_3, WO_3(A), and WO_3(S). i) Corresponding band gaps from UV–vis–NIR spectra.

intensity at a g factor is 116 for WO_3, 171 for WO_3(A), and the most robust signal is observed in WO_3(S) at 227. Following the XPS spectra, the signal intensity is stronger for tungsten oxide with a higher concentration of oxygen vacancies. Figure 3h presents the ultraviolet-visible-near infrared (UV–vis–NIR) absorption spectra of tungsten oxides, providing insights into the optical characterization influenced by oxygen vacancies. The absorption bands of all tungsten oxides are enhanced from 300 to 480 nm due to their intrinsic bandgap of 2.6 eV (Figure 3i).[24] On the other hand, the electrons localized in oxygen vacancies form a broadband that absorbs light from 480 to 800 nm due to a small polaron transition between W^{5+} and W^{6+}. The higher concentration of oxygen vacancies in tungsten oxide results in a greater number of polarons formed, leading to increased light absorption in this range.[24b]

2.3. Photoelectrochemical Performances of the Tungsten Oxides for Glycerol Oxidation

The photocurrent of linear sweep voltammetry (LSV) was utilized to determine the optimal concentration of oxygen vacancies generated through heat treatment and surface reactions for maximizing photoelectrochemical oxidation efficiency (Figure S7, Supporting Information). The photoanodes were evaluated using an electrolyte containing 2 M glycerol and 0.5 M Na_2SO_4, adjusted to a pH of 2. The photocurrent density of tungsten oxide remains unchanged during the heat treatment for oxygen vacancy formation until the volume ratio of Ar gas is increased to Ar 4 vol%: O_2 1 vol%. However, when tungsten oxide is heat treated in an Ar gas atmosphere only, the photocurrent decreases, attributed to insufficient crystallization into the WO_{3-x} monoclinic phase. Among

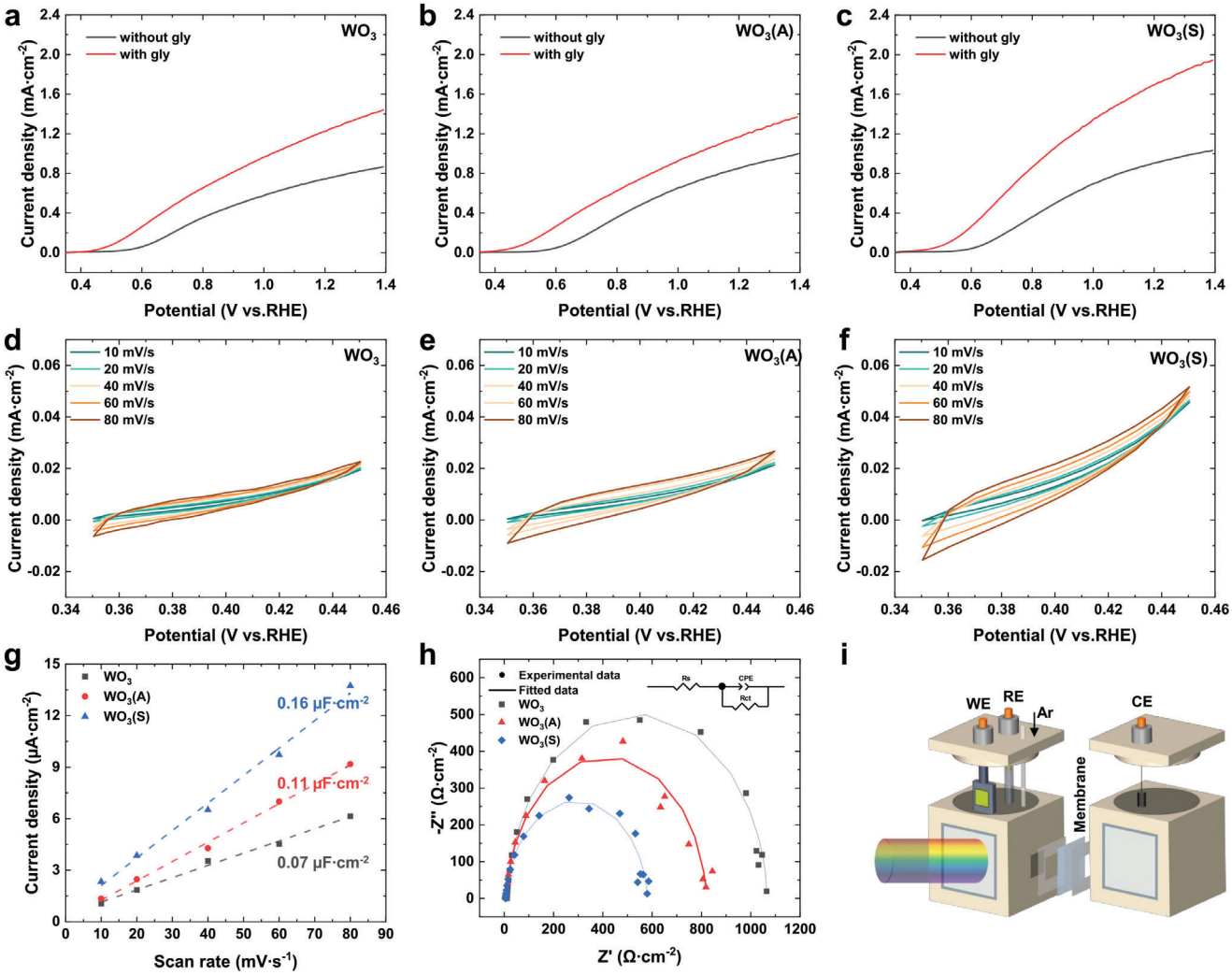

Figure 4. Photoelectrochemical performance analysis in 0.5 M Na_2SO_4 electrolytes, with the pH adjusted to 2 using sulfuric acid. a) LSV profiles of WO_3 with and without 2 M glycerol. b) LSV profiles of WO_3(A) with and without 2 M glycerol. c) LSV profiles of WO_3(S) with and without 2 M glycerol. d) CV curves of WO_3 with 2 M glycerol. e) CV curves of WO_3(A) with 2 M glycerol. f) CV curves of WO_3(S) with 2 M glycerol. g) Corresponding capacitive currents plotted as a function of the scan rate. h) Nyquist plots of WO_3, WO_3(A), and WO_3(S) with 2 M glycerol at a constant potential of 1.2 V_{RHE}. i) Schematic illustration of the photoelectrochemical three-electrode system.

the tungsten oxides that formed oxygen vacancies through surface reaction in $NaBH_4$ at 10, 15, and 30 mM, the tungsten oxide treated at 15 mM exhibited the optimal oxygen vacancy concentration with the highest photocurrent density. The tungsten oxides with the optimal vacancy concentration were then evaluated for their photoelectrochemical performance.

Figure 4 shows that the LSV indicates a higher photocurrent density in the full potential region for WO_3(A) and WO_3(S) compared to WO_3 during the water-splitting reaction in a glycerol-free electrolyte. At 1.2 V_{RHE}, the photocurrent density for WO_3 is 0.74 mA cm^{-2}, while for WO_3(A) and WO_3(S), it is 0.86 and 0.91 mA cm^{-2}, respectively. However, in an electrolyte containing glycerol, which is more thermodynamically oxidizable than water, WO_3(A) shows no significant effect on the photocurrent density, while WO_3(S) results in an explosive increase in current density up to 1.70 mA cm^{-2}. This suggests that surface oxygen vacancies effectively facilitate charge transfer to the glycerol. The decrease in charge transfer resistance, demonstrated by the shrinking of the electrochemical impedance spectroscopy (EIS) circle in Figure 4h, along with the increase in electrochemical activation surface area, as demonstrated by the broader cyclic voltammetry (CV) shape in Figure 4, indicates an improvement in charge transfer capability.[25] WO_3(S) exhibits the smallest charge transfer resistance of 575 Ω cm^{-2} and the largest double layer capacitance of 0.16 μF cm^{-2} (Figure 4g). WO_3(A) also exhibits an enhanced charge transfer capability compared to WO_3. Nevertheless, the expansion of the amorphous region, depicted in the red dashed area in Figure S3d (Supporting Information), resulting from oxygen vacancies in the bulk, leads to charge trapping and diminishes the enhancement of photocurrent by glycerol. Therefore, WO_3(S) stands out as the most suitable structure for photoelectrochemical glycerol oxidation, characterized by the optimal concentration of oxygen vacancies exclusively on the surface. To confirm the stability of the photoelectrochemical oxidation of

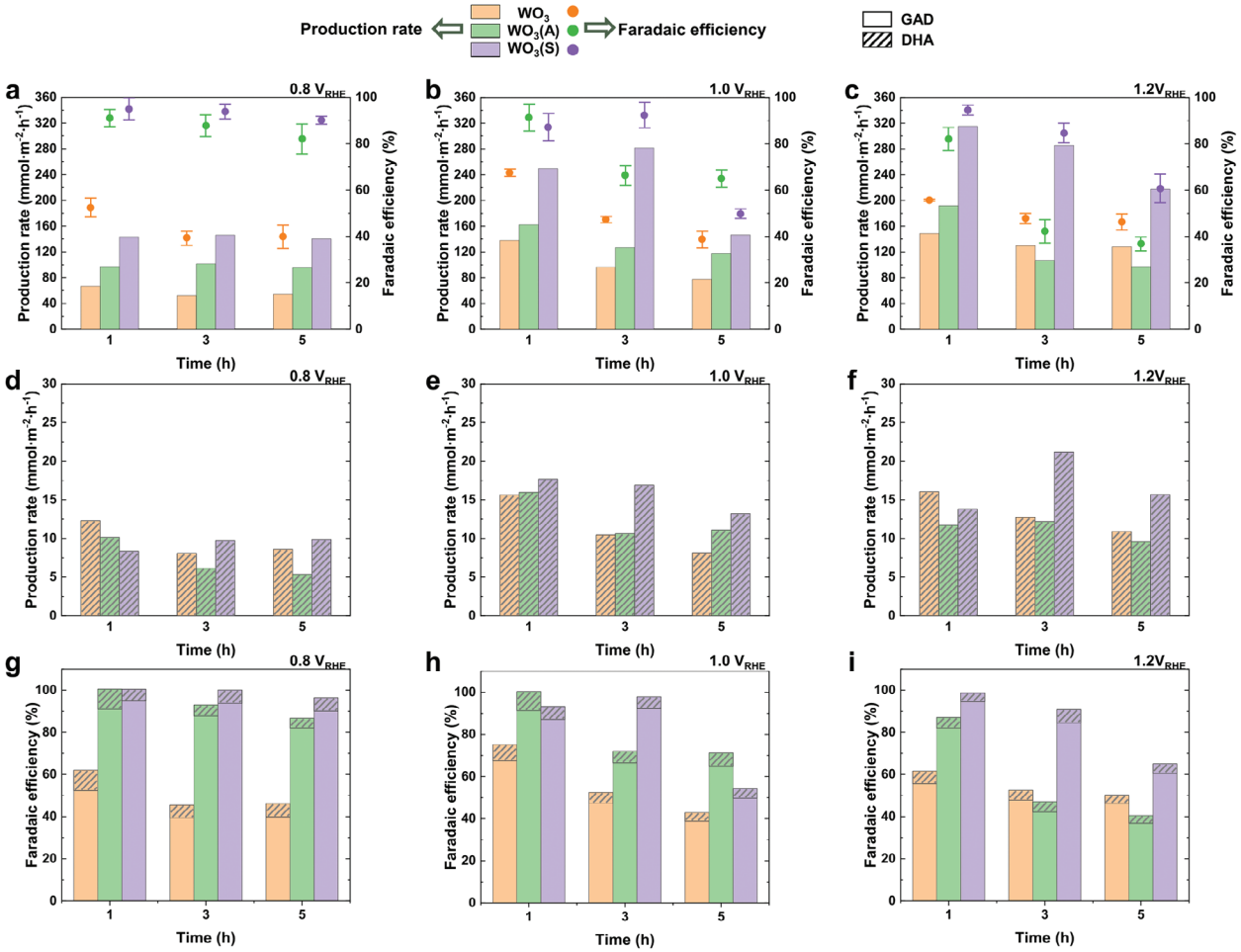

Figure 5. Production rate of GAD from WO_3, WO_3(A), and WO_3(S) at different applied potentials and times: a) 0.8 V_{RHE} b) 1.0 V_{RHE} c) 1.2 V_{RHE}. Production rate of DHA from WO_3, WO_3(A), and WO_3(S) at different constant potentials and times: d) 0.8 V_{RHE} e) 1.0 V_{RHE} f) 1.2 V_{RHE}. Faradaic efficiency of glycerol oxidant product at different constant potentials and times: g) 0.8 V_{RHE} h) 1.0 V_{RHE} i) 1.2 V_{RHE}.

glycerol, each tungsten oxide was measured for 1, 3, and 5 h after electrolyte replenishment, measured successively at a constant potential (Figure S8, Supporting Information). The photocurrent density increased by photoactivation, regardless of the bias potential during the first hour of the reaction, and it remained stable for 3 and 5 h. A nafion membrane partitioned the working electrode and counter electrode to prevent the oxidation products from being affected by the reduction reaction (Figure 4i).

2.4. Quantitative Analysis of Glycerol Oxidant Product

The electrolyte resulting from the oxidation was quantitatively analyzed using both high-performance liquid chromatography (HPLC) and nuclear magnetic resonance (NMR) to confirm the selective conversion of glycerol to GAD. To ensure accurate quantification, we prepared a calibration curve using standard materials of glycerol oxides (Figure S9, Supporting Information). **Figure 5** and Table S2 (Supporting Information) present the quantity of GAD and DHA produced by the tungsten oxides during the conversion of glycerol, along with their respective faradaic efficiencies. WO_3(A) and WO_3(S), with surface vacancies, exhibit high selectivity in producing GAD, ≈90% for 1 and 3 h. The maximum yield of GAD formation is achieved when utilizing WO_3(S) at 1.2 V_{RHE} for 1 h, reaching a yield of 315.1 mmol m^{-2} h^{-1}. In addition to the highly selective formation of GAD, DHA was the predominant remaining product, with no other by-products observed. This indicates that tungsten oxide can selectively convert glycerol to glycerylaldehyde, regardless of the bias potential, as long as oxygen vacancies are adequately formed on the surface. Unfortunately, the selectivity decreases significantly as the reaction progresses, except at 0.8 V_{RHE}, where the bias potential is low and glycerol conversion occurs slowly.

2.5. Investigation of the Electrode Surface for Long-Term Selective Glycerol Oxidation

To address the issue of non-selective conversion of glycerol to GAD over prolonged reaction times, the relationship between selectivity and electrode changes induced by photoelectrochemical reactions was investigated. **Figure** 6a,c, and Table S1 (Sup-

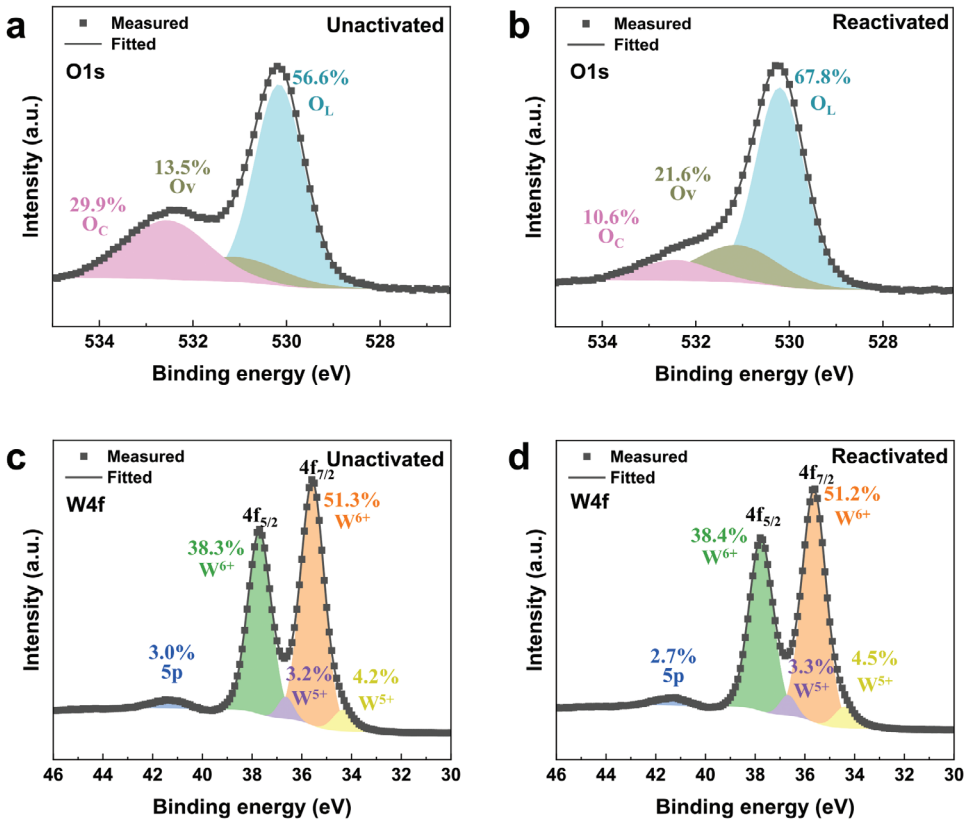

Figure 6. High-resolution O1s XPS spectra of WO_3 (S) after 3 h of photoelectrochemical reaction: a) without surface restoration and b) with surface restoration. High-resolution W4f XPS spectra of WO_3 (S) after 3 h of photoelectrochemical reaction: c) without surface restoration and d) with surface restoration.

porting Information) present the high-resolution XPS results of WO_3 (S) after 3 h of photoelectrochemical reaction, demonstrating the surface changes of the photoelectrode induced by the reaction. The decrease in the O_V concentrations to 13.5% and increase in the O_C concentrations to 29.9% indicates a reduction in oxygen vacancies on the electrode surface due to the adsorption of water (Figure 6a).[15a] The decrease in oxygen vacancy concentration leads to a change in the ratio of W^{5+} to W^{6+} in the W4f orbitals, with W^{5+} decreasing from 8.1% to 7.6% (Table S1, Supporting Information). Although the photoelectrochemical reaction reduces the concentration of oxygen vacancies, the intensity of the ESR signal increases, likely due to the localization of excess electrons at the Brønsted acid sites and vacancy sites (Figure S10, Supporting Information).[26] Therefore, the high surface concentration of chemisorbed oxygen and Brønsted acid sites reduces the available active sites of W^{5+} for glycerol adsorption, thereby diminishing the selectivity of glycerol conversion to GAD.

To reinstate the selective reaction, surface restoration through the reduction reaction of WO_3 by light under bias-free conditions was employed to eliminate adsorbed water and Brønsted acid site, thereby restoring oxygen vacancy sites. Tungsten oxide is an n-type semiconductor with excellent electron mobility (12 $cm^2\ V^{-1}\ s^{-1}$) and a high electron concentration as the majority carrier.[27] When tungsten oxide is exposed to light in an unbiased system, with its surface in contact with an electrolyte, photons induce the separation of electrons and holes. This separation generates a small reductive current in the μA range as the excited electrons interact with the surface. The reductive current primarily interacts with Brønsted acid sites, inducing water desorption.[28] This leads to the transition of W^{6+}, associated with water and Brønsted acid sites, to the W^{5+} state. After a 30-min self-recovery process, O_C was decreased from 29.9% to 10.6% and O_V was restored from 13.5% to 21.6% (Figure 6b). Figure 6d further indicates that the oxygen vacancies are restored, and the W^{5+} ratio between W4f orbitals also returns to 8.0%, approaching its initial value (Table S1, Supporting Information). This recovery effect is evident in the ESR spectrum shown in Figure S10 (Supporting Information). Although the concentration of oxygen vacancies increased on the surface, the ESR signal returned to its initial level as Brønsted acid sites were used to desorb water.

Furthermore, in photoelectrochemical reactions, the enhancement of photocurrent through surface activation observed in the initial reaction can identify a return to the initial state (**Figure** 7a,b). In metal oxide photoelectrodes after photoelectrochemical reactions, the presence of Brønsted acid sites, particularly protonated bridging oxygen plays a critical role in influencing the activity and mechanisms involved in dehydration, isomerization, and cracking reactions.[29] Moreover, in acidic environments, proton adsorption energy at cross-linked oxygen sites enhances proton mobility on the catalyst surface. This facilitates

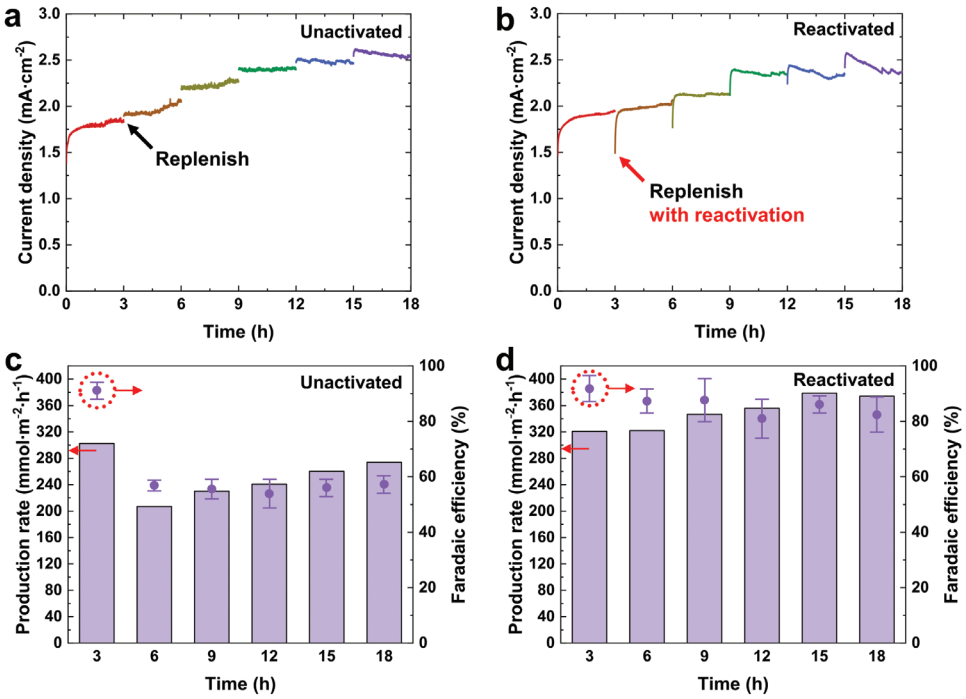

Figure 7. Choronoamperometry of WO_3(S): a) without surface restoration and b) with surface restoration. Production rate of GAD from WO_3(S): c) without surface restoration and d) with surface restoration.

a rapid oxygen-assisted deprotonation process, thereby accelerating oxidation kinetics. The photoelectrochemical activation maximizes photocurrent density, as the interruption of the continuous reaction allows the surface to rearrange and stabilize.[30] Therefore, for the non-self-healing tungsten oxide photoanode, the photoelectrochemical reaction continues, with Brønsted acid sites on the surface maintaining the enhanced photocurrent density. In contrast, for the self-healing tungsten oxide photoanode, the photocurrent density recovers to its initial value by removing the Brønsted acid sites. In terms of self-healing via electrochemical reactions, excessive self-healing for 60 min causes a significant reduction in photocurrent density due to surface damage from the over-reduction of tungsten oxide (Figure S11, Supporting Information). However, with insufficient self-healing for 15 min, the photocurrent density remains higher, showing minimal change compared to the pre-healing state. Therefore, when electrolytes were replenished every three hours without electrode recovery, selectivity decreased from 91.4% to 56.9% over three hours and remained thereafter by surface concentration ratio diminish of W^{5+} and increase of Brønsted acid sites and water (Figure 7c; Table S3, Supporting Information). However, in the conversion of the recovered WO_3(S) to expose W^{5+} sites with replenished electrolytes, the selectivity averaged 86.1% over 18 h (Figure 7d). Maintaining selectivity while enhancing photoelectrochemical performance results in a photocurrent density of 2.58 mA cm^{-2} and a production rate of 378.8 mmol m^{-2} h^{-1}. Figure S12 (Supporting Information) demonstrates oxygen vacancy restoration and W^{5+} site exposure via self-healing after repeating the 3 h reaction for 6 cycles, indicating that this mechanism remains effective even after prolonged periods. As shown in Table S4 (Supporting Information), our photoanode achieves a production rate of GAD, one of the most valuable glycerol oxidation products, using a novel strategy that delivers results comparable to the world record.[8,31] Furthermore, the highest selectivity for DHA or GAD, the C3 products of glycerol, was also achieved. To the best of our knowledge, this approach demonstrates not only the highest selectivity but also the longest operational stability in the world.

2.6. Mechanistic Study on Glycerol Oxidation

To elucidate the mechanism underlying the selectivity difference, the adsorption configurations and reaction energy pathways of glycerol oxidation on WO_3 (without oxygen vacancy) and WO_3 (O_V, with oxygen vacancy) were examined using Density Functional Theory (DFT) calculations in **Figure 8**a. The conversion processes from glycerol to GAD are shown in Figure 8, while the structures of WO_3 and $WO_3(O_V)$ are presented in Figure S13 (Supporting Information). Initially, glycerol adsorbs onto the tungsten oxide surface. The dehydrogenation of glycerol occurs through the acceptance of holes, and the resulting terminal radical reacts with water, forming an unstable intermediate that spontaneously dehydrates to yield GAD. The results indicate that the terminal hydroxyl group of glycerol is adsorbed on both surfaces. The adsorption energy of glycerol on $WO_3(O_V)$ (−1.06 eV) is lower than on WO_3 (0.24 eV). In the subsequent oxidation step, the activation energy barrier is lower on the $WO_3(O_V)$ surface (5.39 eV) compared to the WO_3 surface (5.87 eV). The unstable intermediate undergoes a spontaneous hydration process, followed by dehydration, wherein $WO_3(O_V)$ exhibits a reduced energy barrier compared to WO_3. During the production of the final GAD

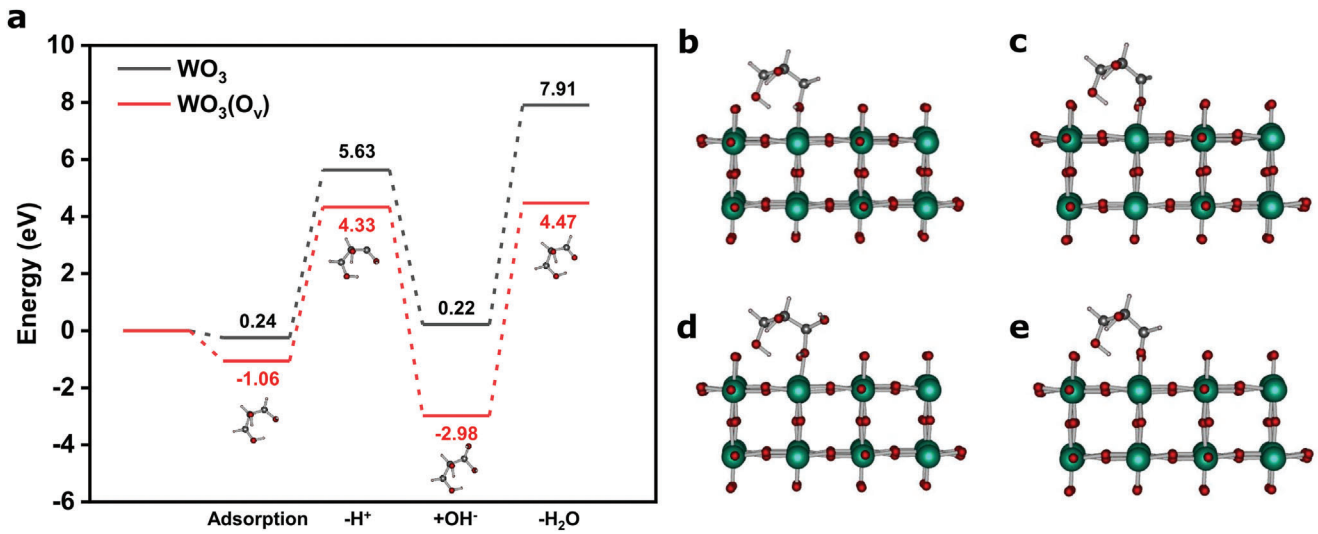

Figure 8. a) Reaction energy pathway of glycerol oxidation on bare WO_3 (100) without oxygen vacancy (O_V) and with O_V. The scheme of conversion processes is shown in b) adsorption on the tungsten oxide surface, c) H desorption, d) hydroxyl adsorption, and e) GAD formation. The red sphere represents oxygen, the green sphere represents tungsten, the gray sphere represents carbon, and the white sphere represents hydrogen.

product, the activation energy on $WO_3(O_V)$ (7.49 eV) is also lower than WO_3 (7.69 eV). Consequently, these results illustrate that the conversion of glycerol to GAD is more efficient on $WO_3(O_V)$ than on WO_3 at each reaction step. This underscores the critical role of oxygen vacancies in enhancing the glycerol to GAD conversion during the oxidation reaction, as GAD faradaic efficiency is higher in WO_3(A) and WO_3(S) with higher oxygen vacancy concentrations compared to WO_3 with lower oxygen vacancy concentrations on the surface (Figure 5). The importance of oxygen vacancies is further emphasized during prolonged reactions, as water and Brønsted acid sites on the surface replace oxygen vacancies (Figure 6). Therefore, by understanding the significance of surface oxygen vacancies in tungsten oxide and utilizing the optimal oxygen vacancy concentration along with its self-recovery capability, glycerol can be selectively converted to GAD over extended periods.

3. Conclusion

In summary, we synthesized tungsten oxide nanostructures with modified oxygen vacancy concentrations for photoelectrochemical glycerol oxidation. The effects of the oxygen vacancy concentration on the photoelectrochemical activity for the oxidation of glycerol to glyceraldehyde were investigated through a combination of experiments and calculations. The photoelectrochemical results elucidate that surface-coordinated tungsten oxides selectively convert glycerol to glycerylaldehyde with high charge transfer efficiency and favorable adsorption capacity for glycerol. The self-healing capability of tungsten oxide is effectively utilized to restore the surface state altered by photoelectrochemical oxidation to its initial state, thereby maintaining its selective conversion of glycerol to glyceraldehyde. This work provides a cornerstone for designing highly efficient metal oxides by modifying the surface oxygen state to enhance selectivity for the photoelectrochemical oxidation of biomass over extended periods.

4. Experimental Section

Fabrication of the Tungsten Oxide: The precursor solution is prepared by mixing 30 mL of deionized water (DI) containing 3 mmol of sodium tungstate dihydrate with 10 mL of 3 M HCl. The solution is left at room temperature (RT) for 30 min, inducing the precipitation of tungstic acid. Then, add 30 mL of DI containing 6 mmol of ammonium oxalate monohydrate to the precipitated solution. The prepared solution is introduced into a Teflon liner along with the FTO substrate, which has been cleansed through successive 10-min ultrasonic baths in DI, acetone, methanol, and isopropyl alcohol, followed by a 20-min UV ozone treatment. The substrate is positioned with its conductive side facing the wall. Teflon liner is sealed in a stainless steel autoclave to maintain the high temperature and pressure of the solution inside. Hydrothermal synthesis involves a reaction in a forced convection oven at 160 °C for 6 h, succeeded by natural cooling to RT for 12 h. The synthesized materials were extracted from the Teflon liner, washed with DI, and then dried in an oven maintained at 60 °C. The material was annealed in a vacuum furnace, starting from RT and increasing at a rate of 5 °C min^{-1}, until reaching 550 °C, where it was maintained for 2 h. In order to regulate the concentration of oxygen vacancies within the bulk, the flow rate of O_2 (99.99%) and Ar (99.99%) gases in the furnace was adjusted while maintaining equal pressure. The Ar-to-O_2 gas ratio was adjusted to 1 vol%:0 vol% (1 mol%:0 mol%), 4 vol%:1 vol% (0.76 mol%:0.24 mol%), and 1 vol%:4 vol% (0.17 mol%:0.83 mol%) to modulate the tungsten oxide vacancies. On the other hand, tungsten oxide underwent a $NaBH_4$ solution to facilitate the formation of oxygen vacancies on the surface. Once the reaction with a 100 rpm magnetic bar is complete, the tungsten oxide is rinsed with deionized water and subsequently dried in an oven set at 60 °C. The concentration of vacancies was modulated by the $NaBH_4$ concentration to 10, 15, and 30 mM while maintaining a constant reaction time of 30 min.

Treatment for Characterization: To utilize tungsten oxide as the photoanode for photoelectrochemical measurements, a connection between a Cu wire and FTO was established using silver paste. Subsequently, after the silver paste had dried at RT, the FTO and Cu wire were encapsulated with epoxy resin to provide separation between the electrodes and the electrolyte. Pyridine adsorption was performed on the tungsten oxide to investigate the surface acid sites. The tungsten oxide and pyridine were allowed to adsorb for 1 h at RT, after which they were dried at 60 °C in an oven to eliminate any unadsorbed pyridine from the tungsten oxide.

Material Characterization: The structural characteristics of the tungsten oxide were determined via XRD (SmartLab, Rigaku) with Cu Kα radiation (λ = 1.5406 Å) and Raman spectroscopy (Renishwa, inVia Raman microscope) with a 514 nm Ar ion laser. To confirm the nanostructure morphology, field-emission SEM (Verios 5 UC, Thermo Fisher Scientific) images were acquired. High-angle annular dark-field scanning transmission electron microscopy images were acquired using High-Resolution Cs-TEM (JEM-ARM300F2, Jeol). The elemental composition of tungsten oxide was analyzed by an XPS (NEXSA, Thermo Fisher Scientific) system. The presence of oxygen vacancies in the tungsten oxide was examined using an ESR (JES-FA100, Jeol). The surface acidity of tungsten oxide was determined via an FTIR spectrometer (Vertex 70v, Bruker). UV–vis absorption spectra of the photoanodes were obtained using the transmission mode of UV–vis spectrophotometer (LAMBDA 950, Perkin Elmer).

Photoelectrochemical Measurements: Electrochemical characteristics were investigated using a potentiostat (Ivium-n-Stat, Ivium Technologies) with a 150 W Xe lamp (Model 10 500, ABET Technology). The light intensity was calibrated at 1-sun intensity (100 mW cm^{-2}) using a photodiode (Bunkokeiki Co., Ltd.). All photoelectrochemical measurements were conducted within a three-electrode system, situated in an H-type quartz cell, wherein the working electrode and counter electrode were partitioned by a Nafion membrane. The electrodes were constructed with tungsten oxide, a standard calomel electrode (SCE), and a platinum coil for the working, reference, and counter electrodes, respectively. The potentials, relative to the SCE electrode, were converted to the reversible hydrogen electrode (RHE) using the Nernst equation; $E_{RHE} = E_{SCE} + 0.059 \times pH + 0.241$, where E_{RHE} is the converted potential, and E_{SCE} is the reference potential of the SCE electrode. The pH of 0.5 M Na_2SO_4 electrolytes was calibrated to 2 using sulfuric acid, irrespective of the presence of 2 M glycerol. LSV was performed with a scan rate of 20 mV s^{-1} and a scan step size of 10 mV. EIS was performed at potentials of 1.2 V_{RHE}, in a frequency range of 100 kHz to 0.1 Hz under illumination. The CV was conducted at a potential from 0.35 to 0.45 V_{RHE} at scan rates of 10, 20, 40, 60, 80, and 100 mV s^{-1} with 2 M glycerol.

Quantification Analysis: The quantification of products was performed using HPLC (Alliance 2695, Waters) systems, equipped with an Aminex HPX 87-H column (9.0 µm, 300 mm × 7.8 mm, Bio-Rad) and a UV detector (waters 2487, waters). The column temperature was consistently maintained at 60 °C, and the UV detector wavelength was set at 210 nm for the detection of oxidation products. A 20 µL sample of the electrolyte, where the oxidation occurred, was injected into the HPLC system using isocratic elution with 5 mM sulfuric acid at a flow rate of 0.6 mL min^{-1}. NMR (JNM-ECX400, Jeol) was utilized to supplement the qualitative analysis using deuterium oxide. The faradaic efficiency (η) of the liquid products was calculated using the following equation; Faradaic efficiency = $\frac{z \times mol \times \frac{V}{u}}{Q}$, where mol is the number of moles of liquid products, V is the total volume of the electrolyte, u is the injection volume of HPLC, and Q is the total charge passed through the electrode. The z value of GAD and DHA is 2, according to the following reaction formula; Glyceraldehyde & Dihydroxyacetone (GAD/DHA): $C_3H_8O_3 \rightarrow C_3H_6O_3 + 2H^+ + 2e^-$.

Computational Details: First-principles calculations were performed using Quantum Espresso with the DFT method. The projector-augmented-wave method was employed to describe the interactions between valence electrons and ion cores. The exchange-correlation potential was treated using the Perdew–Burke–Ernzerhof functional within the generalized gradient approximation. 2 × 2 × 1 supercell was used to generate the (001) crystal planes for simulating various catalyst surfaces. To prevent interlayer interactions, a 15 Å vacuum layer was introduced along the Z-axis. The plane-wave basis set cutoff energy was 38.22 Ry, and a 2 × 2 × 1 Monkhorst-Pack grid was used for the Brillouin zone. For geometry optimization, the energy convergence criterion was set to 1.0 × 10^{-6} Ry/bohr, and the force convergence threshold was set to 0.0005 Ry. The adsorption energy (E_{ads}) between the surface and the adsorbed molecules was calculated as follows; $E_{ads} = E_{surface+molecule} - E_{surface} - E_{molecule}$.

Supporting Information

Supporting Information is available from the Wiley Online Library or from the author.

Acknowledgements

Y.J. and S.K. contributed equally to this work. This research was funded by the "National Research Foundation of Korea (NRF)", a grant funded by the Korean government (MSIT) No. 2021R1A5A1028138. This research was supported by the program of Future Hydrogen Original Technology Development (2021M3I3A1084747), through the National Research Foundation of Korea (NRF), funded by the Korean government (Ministry of Science and ICT(MSIT)). This work was supported by the GIST-MIT Research Collaboration grant funded by the GIST.

Conflict of Interest

The authors declare no conflict of interest.

Data Availability Statement

The data that support the findings of this study are available from the corresponding author upon reasonable request.

Keywords

glycerol, long-term, photoelectrochemical, selectivity, vacancy

Received: October 4, 2024
Revised: October 17, 2024
Published online: October 24, 2024

[1] H. Luo, J. Barrio, N. Sunny, A. Li, L. Steier, N. I. Shah, I. E. L. Stephens, M. M. Titirici, *Adv. Energy Mater.* **2021**, *11*, 2101180.
[2] X. Huang, Y. Y. Guo, Y. Zou, J. Jiang, *Appl. Catal. B.-Environ.* **2022**, *309*, 121247.
[3] H. H. Kuo, T. G. Vo, Y. J. Hsu, *J. Photoch. Photobio C* **2024**, *58*, 100649.
[4] K. Sayama, *ACS Energy Lett.* **2018**, *3*, 1093.
[5] G. Dodekatos, S. Schünemann, H. Tüysüz, *ACS Catal.* **2018**, *8*, 6301.
[6] a) M. A. Vandelli, F. Rivasi, P. Guerra, F. Forni, R. Arletti, *Int. J. Pharm.* **2001**, *215*, 175; b) K. Jung, M. Seifert, T. Herrling, J. Fuchs, *Spectrochim Acta A* **2008**, *69*, 1423.
[7] Y. Liu, B. Zhang, D. P. Yan, X. Xiang, *Green Chem.* **2024**, *26*, 2505.
[8] L. Luo, W. S. Chen, S. M. Xu, J. R. Yang, M. Li, H. Zhou, M. Xu, M. F. Shao, X. G. Kong, Z. H. Li, H. H. Duan, *J. Am. Chem. Soc.* **2022**, *144*, 7720.
[9] Y. Liu, M. Wang, B. Zhang, D. P. Yan, X. Xiang, *ACS Catal.* **2022**, *12*, 6946.
[10] D. W. Chu, H. Zhou, Z. C. Luo, *New J. Chem.* **2022**, *46*, 18744.
[11] T. G. Vo, C. C. Kao, J. L. Kuo, C. C. Chiu, C. Y. Chiang, *Appl Catal B-Environ* **2020**, *278*, 119303.
[12] L. H. Yang, Y. Y. Jiang, Z. H. Zhu, Z. Y. Hou, *Mol. Catal.* **2022**, *523*, 111545.
[13] Y. S. Jung, S. Kim, H. Choi, Y. Kim, J. B. Hwang, D. H. Y. Lee, Y. Kim, J. C. Park, D. Y. Kim, S. H. Lee, *Nanomaterials-Basel* **2023**, *13*, 1690.
[14] Y. Lee, S. Kim, S. Y. Jeong, S. Seo, C. Kim, H. Yoon, H. W. Jang, S. Lee, *Catal. Today* **2021**, *359*, 43.

[15] a) H. J. Kong, H. Yang, J. S. Park, W. S. Chae, H. Y. Kim, J. Park, J. H. Lee, S. Y. Choi, M. Park, H. Kim, Y. Song, H. Park, J. Yeo, *Adv. Funct. Mater.* **2022**, *32*, 2204106; b) Q. Liu, F. J. Wang, H. X. Lin, Y. Y. Xie, N. Tong, J. J. Lin, X. Y. Zhang, Z. Z. Zhang, X. X. Wang, *Catal. Sci. Technol.* **2018**, *8*, 4399.

[16] N. Zhang, X. Y. Li, Y. F. Liu, R. Long, M. Q. Li, S. M. Chen, Z. M. Qi, C. M. Wang, L. Song, J. Jiang, Y. J. Xiong, *Small* **2017**, *13*, 1701354.

[17] a) B. Liu, D. P. Cai, Y. Liu, D. D. Wang, L. L. Wang, Y. R. Wang, H. Li, Q. H. Li, T. H. Wang, *Sensor Actuat B-Chem* **2014**, *193*, 28; b) X. Y. Tang, M. F. Li, L. F. Gao, H. Yan, S. M. Deng, J. B. Fan, M. S. Zheng, S. L. Deng, Q. Y. Zhang, S. Y. Xie, L. S. Zheng, *Adv. Mater. Interfaces* **2019**, *6*, 1901122.

[18] a) W. Q. Song, R. Zhang, X. Bai, Q. Q. Jia, H. M. Ji, *J Mater Sci-Mater El* **2020**, *31*, 610; b) J. J. Diaz-Reyes, E. F.-M., J. M. Gutierrez-Arias, M. M. Morincastillo, H. Azucena-Coyotecatl, M. Galvan, P. Rodriguez-Fragoso, A. Mendez-Lopez, *Advances in Sensors, Signals and Materials* **2010**, *137*, 99.

[19] C. J. Liu, J. M. Sun, H. M. Brown, O. G. Marin-Flores, J. T. Bays, A. M. Karim, Y. Wang, *Catal. Today* **2016**, *269*, 103.

[20] a) H. Tamura, K. Mita, A. Tanaka, M. Ito, *J. Colloid Interf. Sci.* **2001**, *243*, 202; b) L. K. Dhandole, M. A. Mahadik, S. G. Kim, H. S. Chung, Y. S. Seo, M. Cho, J. H. Ryu, J. S. Jang, *ACS Appl. Mater. Interfaces* **2017**, *9*, 23602.

[21] a) F. L. Liu, X. J. Chen, Q. H. Xia, L. H. Tian, X. B. Chen, *RSC Adv.* **2015**, *5*, 77423; b) R. Ji, D. Zheng, C. Zhou, J. Cheng, J. S. Yu, L. Li, *Materials* **2017**, *10*, 820.

[22] M. Quesada-González, N. D. Boscher, C. J. Carmalt, I. P. Parkin, *ACS Appl. Mater. Interfaces* **2016**, *8*, 25024.

[23] J. W. Qian, Z. J. Peng, Z. G. Shen, Z. Y. Zhao, G. L. Zhang, X. L. Fu, *Sci. Rep-UK* **2016**, *6*, 25574.

[24] a) A. K. Mohamedkhair, Q. A. Drmosh, M. Qamar, Z. H. Yamani, *Catalysts* **2021**, *11*, 381; b) Y. Z. Wu, W. Q. Zhou, L. Zhou, S. I. In, J. Y. Lei, L. Z. Wang, J. L. Zhang, Y. D. Liu, *Chem. Eng. J.* **2023**, *474*, 145267.

[25] Q. H. X. Li, Y. Xu, X. Liang, J. Feng, K. Zhao, G. Guan, Y. Jiang, X. Hao, K. Tang, *Carbon Resources Conversion* **2021**, *4*, 76.

[26] a) R. Krzyminiewski, B. Dobosz, G. Schroeder, J. Kurczewska, *Sci. Rep-UK* **2019**, *9*, 18733; b) B. Wang, A. J. Fielding, R. A. W. Dryfe, *J. Phys. Chem. C* **2019**, *123*, 22556.

[27] G. W. Zheng, J. S. Wang, H. Liu, V. Murugadoss, G. N. Zu, H. B. Che, C. Lai, H. Y. Li, T. Ding, Q. Gao, Z. H. Guo, *Nanoscale* **2019**, *11*, 18968.

[28] E. Albanese, C. Di Valentin, G. Pacchioni, *ACS Appl. Mater. Interfaces* **2017**, *9*, 23212.

[29] a) T. H. Li, M. N. Ruan, Z. A. Guo, C. Y. Wang, Z. F. Liu, *ACS Appl. Mater. Interfaces* **2023**, *15*, 11914; b) Y. Z. Wen, C. Liu, R. Huang, H. Zhang, X. B. Li, F. P. G. de Arquer, Z. Liu, Y. Y. Li, B. Zhang, *Nat. Commun.* **2022**, *13*, 4871.

[30] Y. L. Chung, S. Kim, Y. Lee, D. T. Wijaya, C. W. Lee, K. Jin, J. Na, *Iscience* **2024**, *27*, 110383.

[31] a) J. Yu, F. Dappozze, J. Martín-Gomez, J. Hidalgo-Carrillo, A. Marinas, P. Vernoux, A. Caravaca, C. Guillard, *Appl. Catal. B-Environ.* **2021**, *299*, 120616; b) X. H. Li, J. Wang, A. L. Wei, X. H. Li, W. G. Zhang, Y. M. Liu, *Sep. Purif. Technol.* **2024**, *332*, 125779; c) J. Yu, J. González-Cobos, F. Dappozze, F. J. López-Tenllado, J. Hidalgo-Carrillo, A. Marinas, P. Vernoux, A. Caravaca, C. Guillard, *Appl Catal B-Environ* **2022**, *318*, 121843; d) Z. N. Gu, X. Q. An, R. P. Liu, L. Q. Xiong, J. W. Tang, C. Z. Hu, H. J. Liu, J. H. Qu, *Appl Catal B-Environ* **2021**, *282*, 119541; e) J. Ouyang, X. Liu, B. H. Wang, J. B. Pan, S. Shen, L. Chen, C. T. Au, S. F. Yin, *ACS Appl. Mater. Interfaces* **2022**, *14*, 23536; f) X. Y. Feng, X. F. Feng, F. Q. Zhang, *J. Mater. Chem. A* **2023**, *11*, 20242.

